RSC Advances

PAPER

View Article Online
View Journal | View Issue

Cite this: *RSC Adv.*, 2026, **16**, 12524

Tuning the charge distribution of Co–N–C active sites for enhanced trifunctional electrocatalysis

Zhaopeng Sun,†[a] Yaling Wu,†[a] Yingying Chen,[a] Zhibo Li,[a] Sen Lei,[ab] Yongyong Cao,*[a] Lianwen Zhu,[a] Xuebo Cao*[a] and Zheng Yan*[a]

Previous studies have often focused on optimizing electrocatalytic performance by altering the type of metal centers or the morphological structure of catalysts to modulate their electronic structures and active sites. However, the precise regulation of metal valence states to enhance catalytic performance—particularly for trifunctional electrocatalysis in the oxygen reduction reaction (ORR), oxygen evolution reaction (OER), and hydrogen evolution reaction (HER)—remains in the exploratory stage. In this study, crystalline Co–N_6 materials with controllable valence states were carefully selected as precursors. Through carbonization, **Co–N–C** materials with similar carbon frameworks but distinct metal valence states (Co^{2+} and Co^{3+}) were successfully prepared. Both experimental tests and theoretical calculations demonstrate the superior trifunctional electrocatalytic performance of **Co^{2+}–N–C**. Density functional theory (DFT) calculations provide evidence for the more favorable intermediate adsorption energies and lower reaction energy barriers exhibited by **Co^{2+}–N–C**. This performance advantage stems from the $3d^7$ electronic configuration of Co^{2+}, which optimizes electron cloud density and strengthens Co–N bonding interactions. This work presents a new strategy for designing highly efficient electrocatalysts by elucidating the regulatory role of metal valence states.

Received 5th January 2026
Accepted 11th February 2026

DOI: 10.1039/d6ra00087h

rsc.li/rsc-advances

Introduction

Driven by the continuous development of energy conversion and storage technologies, electrocatalytic reactions, including the oxygen reduction reaction (ORR), oxygen evolution reaction (OER), and hydrogen evolution reaction (HER), have become the core driving forces in many fields, such as fuel cells, metal–air batteries, and water electrolysis.[1–6] In the process of these reactions, materials with high electrochemical activity and durability are undoubtedly the key factors for achieving efficient reactions. Noble metal catalysts, such as Pt-based nanomaterials, exhibit excellent bifunctional catalytic properties in the HER and ORR, while Ru-based and Ir-based catalysts perform well in the OER. However, their rarity and high cost have greatly limited their application prospects in large-scale production.[7–16] Therefore, optimizing non-noble inorganic material catalysts to achieve efficient energy conversion is not only a core step in promoting the wide application of new energy storage and conversion technologies but also a significant research challenge currently faced in this field.[17–19]

Currently, researchers' exploration in the field of multifunctional catalysts mainly focuses on two key approaches. On the one hand, they are fully committed to the meticulous design and precise synthesis of highly efficient catalysts with catalytically active centers. On the other hand, they are conducting in-depth analyses of the reaction mechanisms and processes of catalysts, aiming to enhance the comprehensive understanding of catalysts and broaden their application scope.[20–23] Numerous research groups have achieved a series of highly inspiring results in related studies. For example, the research group led by Hao Ming Chen conducted an in-depth investigation into the influence of metal valence states on electrocatalysis in metal oxide systems. They successfully confirmed that CoOOH formed from Co^{2+} serves as the oxidation site for water electrolysis. This discovery highlights the significant role of metal valence states in the formation of key electrocatalytic reaction sites in specific materials.[24] The research group led by Yaping Li took an innovative approach. They ingeniously incorporated $Co^{2+/3+}$ sites into the NiFe-LDH structure and conducted an in-depth investigation into its effect on the OER activity. By simplifying the structure, they demonstrated the efficacy of valence states. The results showed that the performance was significantly improved after Co^{3+} doping.[25] Hu Xile's group elucidated the influence of valence state modulation on the electrocatalytic reduction of CO_2 in Fe^{3+}–N–C catalysts, providing a clear rationale for the development of highly efficient electrocatalysts through valence state engineering.[26]

[a]*College of Biological, Chemical Sciences and Engineering, Jiaxing University, Jiaxing 314001, P. R. China. E-mail: yzheng158@zjxu.edu.cn*

[b]*School of Chemistry and Chemical Engineering, Zhejiang Sci-Tech University, Hangzhou 310018, China*

† These authors contributed equally to this work.

Previous studies indicate that **Co–N–C** catalysts possess notable structural advantages:[27–29] (1) at the atomic level, by meticulously designing the precursor Co–N_6—which enables effective modulation of the metal center properties—allows for the construction of **Co–N–C** materials with precisely controlled cobalt valence states (Co^{2+} or Co^{3+}) through subsequent transformation. Additionally, the carbon substrate itself can provide additional adsorption sites, and the two (*i.e.*, the Co–N active sites derived from Co–N_6 transformation and the adsorption sites on the carbon substrate) synergistically increase the number of active sites. (2) From a structural perspective, **Co–N–C** materials exhibit a two-dimensional planar architecture. Its high specific surface area not only facilitates the rapid access of electrocatalytic reaction substrates (*e.g.*, protons in HER, and O_2 in OER and ORR) to the catalytic sites—thereby effectively increasing the probability of reaction contact[30]—but also shortens the transport pathways for ions and electrons within the material, reduces energy loss, and thus accelerates the kinetic process of electrocatalytic reactions.[31,32] Based on these advantageous properties, this work meticulously selected precursors and successfully synthesized crystalline MOFs featuring Co–N_6 structures with well-defined metal valence states (Fig. 1). Subsequent carbonization under a N_2 atmosphere—effectively suppressing abnormal valence transitions of Co species during pyrolysis and ensuring valence stability—facilitated the directed transformation of the Co–N_6 motifs into **Co–N–C** materials. This process yielded two target catalysts: **Co^{2+}–N–C** and **Co^{3+}–N–C**. Building upon this foundation, we further investigated the influence of charge regulation on the trifunctional electrocatalytic performance of **Co–N–C** catalysts for ORR, OER, and HER. Both experimental measurements and theoretical calculations consistently demonstrated that **Co^{2+}–N–C** exhibits superior catalytic activity and stability across all three reactions. This marked performance disparity clearly establishes the metal center's valence state as a critical factor governing the electrocatalytic efficacy of **Co–N–C** materials. These findings not only provide a new perspective for understanding the structure–activity relationships of MOF-derived electrocatalysts, but also open a promising avenue for optimizing multifunctional electrocatalytic performance through deliberate valence state engineering.

Experimental section

Materials

All analytical-grade chemicals and used as received. $CoCl_2 \cdot 6H_2O$, $Co(CH_3COO)_2 \cdot 4H_2O$, ethyl 1*H*-tetrazole-5-carboxylate (ETC), *N*,*N*-bis[1(2)*H*-tetrazol-5-yl]amine (H_3bta), sodium azide, sodium dicyanamide, hydrochloric acid, absolute ethanol, and isopropanol were obtained from Sinopharm Chemical Reagent Co., Ltd and Shanghai Aladdin Biochemical Technology Co., Ltd. Nafion PFSA polymer (5%) was supplied by Chemours. Distilled water (with a purity exceeding 18 MΩ cm), was purified through a microporous membrane system.

Catalyst synthesis

$[Co(HCN_4)_2 \cdot (H_2O)_{2/9}] \cdot 1.4H_2O$ (denoted as Co^{2+}-MOF-1).[33] $Co(CH_3COO)_2 \cdot 4H_2O$ (49.8 mg, 0.2 mmol) was mixed with ETC (56.8 mg, 0.4 mmol) in 15 mL of distilled water. The mixture was subsequently placed into a polytetrafluoroethylene (PTFE) container and maintained at 125 °C for a duration of 20 h. The product was filtered, rinsed multiple times with ethanol, and vacuum-dried at 50 °C for 12 h. The precursor **Co^{2+}-MOF-1** was thus prepared with a yield of approximately 70%.

$Co(HBTA)_3 \cdot 4.5H_2O$ (denoted as Co^{3+}-MOF-2).[34] $CoCl_2 \cdot 6H_2O$ (23.8 mg, 0.1 mmol) and H_3bta (45.9 mg, 0.3 mmol) were dissolved and combined in 50 mL of distilled water. The mixture was subsequently placed into a PTFE container and maintained at 125 °C for a duration of 20 h. The resulting clear mixed solution was filtered, and the filtrate was placed in a sealed

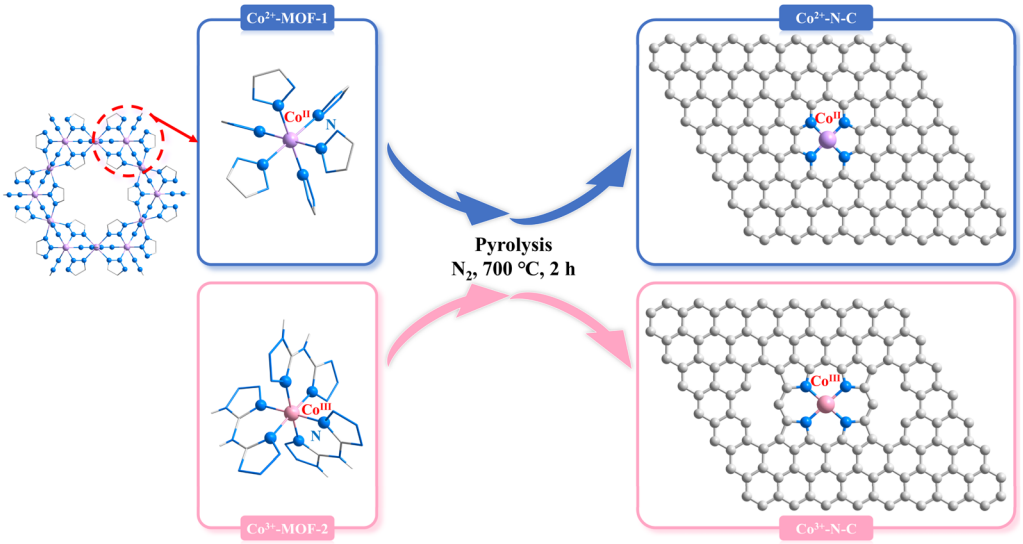

Fig. 1 Schematic diagram of the synthesis of Co^{2+}–N–C and Co^{3+}–N–C from Co^{2+}-MOF-1 and Co^{3+}-MOF-2, respectively (with metal valence centers of Co^{2+} and Co^{3+}).

environment at 6 °C for slow crystallization. Pink crystals precipitated out. After being washed with ethanol and dried, the precursor **Co^{3+}-MOF-2** was finally prepared with a yield of approximately 34%.

Carbonization of precursors.[35] A 200 mg sample of **Co^{2+}-MOF-1** precursor was loaded into a tube furnace within a magnetic boat for calcination. The precursor was heated to 700 °C (5 °C min^{-1}) under a N_2 atmosphere and held at that temperature for 2 h. Upon reaching room temperature naturally, the product was retrieved, stirred in 1 M HCl overnight, washed with distilled water until neutrality (pH ≈ 7), and dried under vacuum at 50 °C for 24 h. The resulting sample was named **Co^{2+}–N–C**. Prepare **Co^{3+}–N–C** following the same steps, except that the precursor is replaced with **Co^{3+}-MOF-2**.

Results and discussion

Characterization of structural properties of Co^{2+}–N–C and Co^{3+}–N–C

First, the sample catalysts were characterized by powder X-ray diffraction (PXRD) to analyze their crystal phases and structures. From the PXRD pattern of the synthesized precursor (details see Fig. S1), it can be found that the diffraction peaks of **Co^{2+}-MOF-1** correspond one-to-one to the peak positions of the simulated pattern of Co^{2+}-MOF-simulated,[33] indicating that it conforms to the structure of $[Co(HCN_4)_2 \cdot (H_2O)_{2/9}] \cdot 1.4H_2O$. In contrast, the diffraction peaks of **Co^{3+}-MOF-2** can be well-matched with those of Co^{3+}-MOF-simulated (CCDC 661223), which means that it meets the structural characteristics of $Co(HBTA)_3 \cdot 4.5(H_2O)$.[34] Additionally, the thermogravimetric analysis combined with differential scanning calorimetry (TG-DSC) results (as shown in the supplementary Fig. S2) indicate that the synthesized precursor **Co^{2+}-MOF-1** stabilizes in mass and ceases to change after the temperature rises to 620 °C, while **Co^{3+}-MOF-2** reaches a constant mass after attaining 550 °C. Taking into account the heat resistance of the materials as well as the structural characteristics of the target product, 700 °C was selected as the carbonization temperature. Under these temperature conditions, the precursors **Co^{2+}-MOF-1** and **Co^{3+}-MOF-2** with different valence states were subjected to carbonization treatment under nitrogen protection. Benefiting from the inert nature of nitrogen, the organic ligands of the precursors were fully decomposed during the carbonization process, allowing the metal ions to effectively react with the nitrogen source. Consequently, **Co–N–C** materials with specific structures and performance characteristics were successfully constructed (Fig. 1). These materials were able to stably maintain the original valence states of their precursors.[35,36] The PXRD patterns of **Co^{2+}–N–C** and **Co^{3+}–N–C** catalysts (Fig. 2a) revealed prominent diffraction peaks at $2\theta \approx 24.3°$ matched the (002) plane of graphitic carbon, indicating the presence of graphitized structures in the synthesized material.[37,38] This feature implies that the material exhibits a graphite-like layered structure at the microscopic level, which, with its unique electron delocalization properties and well-ordered layered structure, usually contributes positively to the enhancement of the material's electrical conductivity and other related properties.[39]

Raman spectroscopy was employed to conduct a more in-depth analysis of the graphitization degree and defect features of the two **Co–N–C** catalysts. As shown in Fig. 2b, both **Co^{2+}–N–C** and **Co^{3+}–N–C** materials with distinct metal valence states display prominent peaks at 1340 cm^{-1} and 1588 cm^{-1}, representing the D-band and G-band of carbon materials, respectively.[40] Specifically, the D-peak represents the characteristic vibration mode of sp^3 defect sites in carbon atoms, while the G-peak reflects the vibration of sp^2-bonded atoms. Notably, the intensity ratio I_D/I_G of these two peaks can serve as a key indicator of the degree of graphitization as well as the defect density of the material.[41] Through the integral fitting process of the spectra, the I_D/I_G values of **Co^{2+}–N–C** and **Co^{3+}–N–C** were found to be 1.21 and 1.32, respectively. Generally, a lower I_D/I_G value indicates that the corresponding material has a better graphitization level, which is more beneficial for the efficient transmission of electrons.[42] This conclusion is also consistent with the intensity of the relative carbon peak (002) lattice plane shown in the PXRD data. The structural characteristics of the material before and after carbonization were characterized and analyzed by Fourier transform infrared (FT-IR) technology. In Fig. 2c, the FT-IR spectra of the precursors **Co^{2+}-MOF-1** and **Co^{3+}-MOF-2** are presented. The two curves have their own characteristic peaks at different wavenumbers. When we focus on the FT-IR spectra of carbonized **Co^{2+}–N–C** and **Co^{3+}–N–C** in Fig. 2d, the spectral profiles of both materials exhibit similar peak positions, peak shapes, and relative intensities at several key wavenumber positions over a range of wavenumbers from 4000 cm^{-1} to 400 cm^{-1}. During the carbonization process, this fully indicates that the **$Co^{2+/3+}$–N–C** materials generated from the two precursors have significant similarities in chemical structure, which provides a solid foundation for the subsequent in-depth investigation of the structure–activity relationship between their properties and structures.

The morphological and microstructural features of the two catalysts were systematically characterized using scanning electron microscope (SEM) and transmission electron microscopy (TEM). SEM results reveal that **Co^{2+}–N–C** exhibits a uniformly distributed cubic morphology (Fig. 3a–c) with an average particle size of approximately 100 nm. The abundant interstitial voids between particles are conducive to enhanced mass transport during electrocatalytic reactions.[43] In contrast, **Co^{3+}–N–C** predominantly displays an irregular rod-like morphology (Fig. 3d–f) with significantly larger particle dimensions, averaging around 500 nm. TEM images in Fig. S3a and e reveal that **Co^{2+}–N–C** exhibits a more homogeneous structure with smaller particle sizes and an ordered arrangement, in contrast, **Co^{3+}–N–C** has significantly larger particle sizes with a relatively loose distribution. Corresponding energy-dispersive spectroscopy (EDS) elemental mapping (Fig. S3b–d and f–h) confirms the successful doping and uniform distribution of Co, N, and C in both materials. Notably, nitrogen in **Co^{2+}–N–C** demonstrates a higher distribution uniformity, suggesting a more regular arrangement of active sites that contributes to its superior electrocatalytic performance.

Furthermore, X-ray photoelectron spectroscopy (XPS) will be used to further analyze the elemental composition and

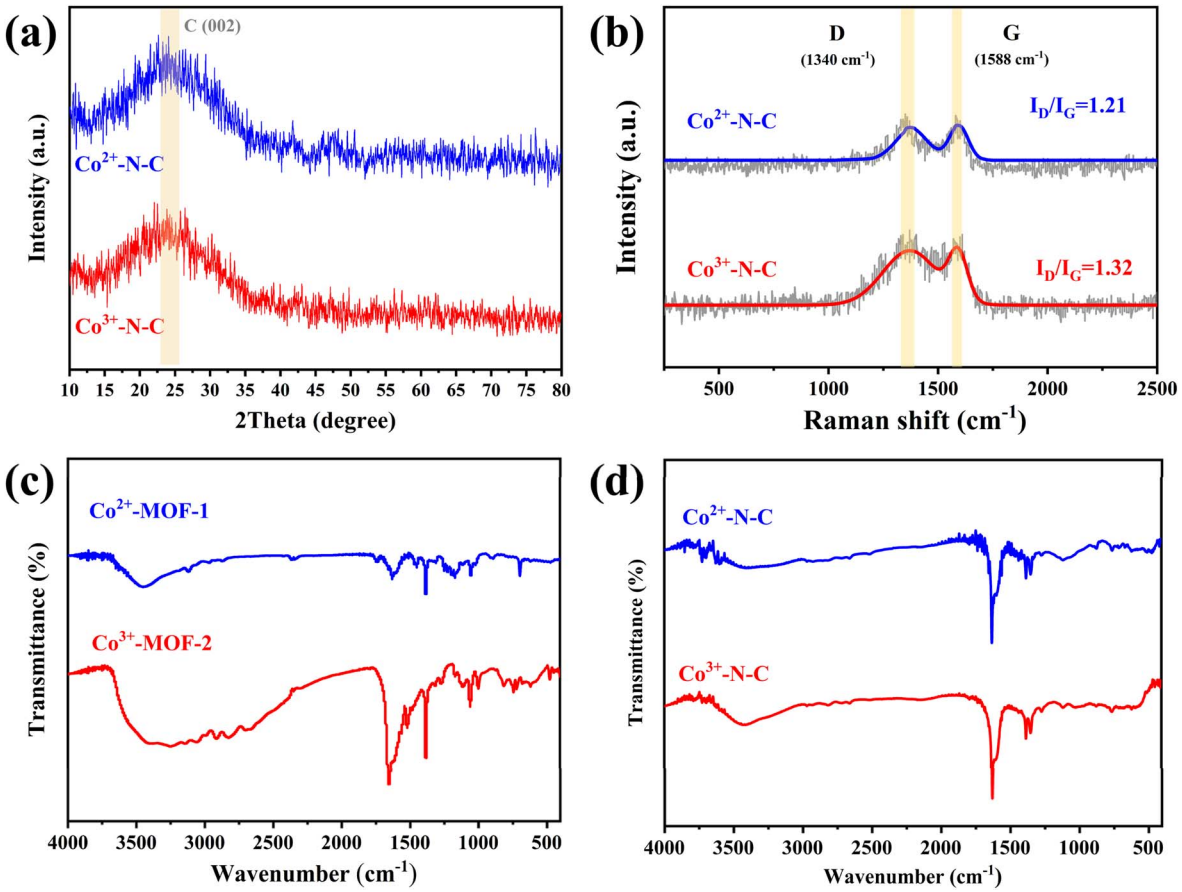

Fig. 2 $Co^{2+/3+}$–N–C catalysts: (a) PXRD comparison spectra; (b) Raman comparison spectra; (c) IR spectra of Co-MOF precursors with different metal valence centers; (d) IR spectra of Co–N–C catalysts with different metal valences.

coordination environment of the **Co–N–C** catalyst. Evidently, as demonstrated by the full spectrum presented in Fig. 4a, the characteristic signals corresponding to Co, O, N, and C can be significantly captured. Specifically, the Co 2p XPS spectrum of the **Co^{2+}–N–C** material (Fig. 4b) shows two main peaks at approximately 780.36 eV and 796.10 eV, which are assigned to Co^{2+} $2p_{3/2}$ and Co^{2+} $2p_{1/2}$, respectively. Their binding energy positions agree well with those reported in ref. 44 The presence of distinct satellite peaks (Sat.) adjacent to these main peaks further confirms the existence of Co^{2+} species. Meanwhile, in **Co^{3+}–N–C** materials, the signals located around 779.15 eV and 794.51 eV should be attributed to the Co^{3+} $2p_{3/2}$ and Co^{3+} $2p_{1/2}$ energy levels.[45] In the **Co–N–C** material system, the unique coordination mode between nitrogen and cobalt atoms exerts

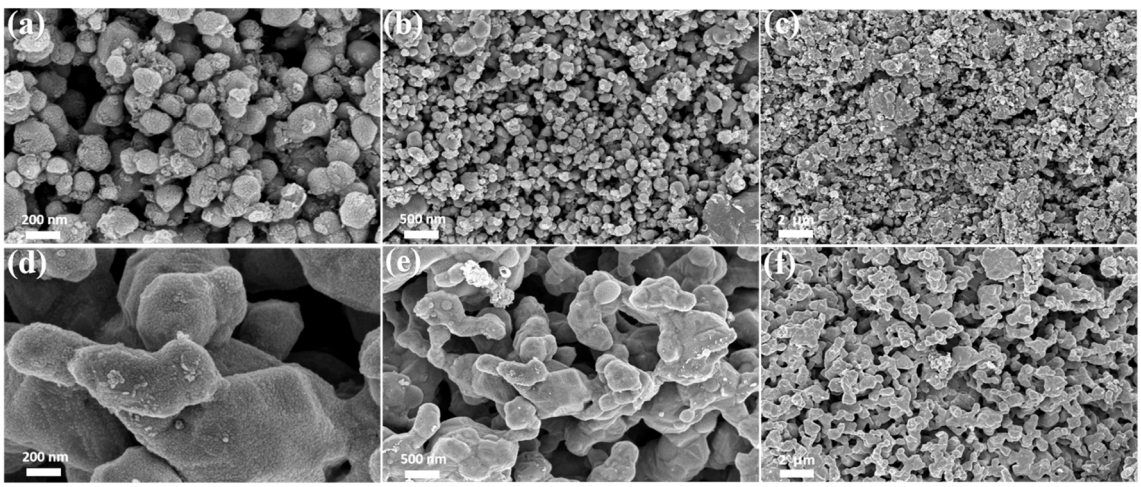

Fig. 3 (a–c) SEM images of **Co^{2+}–N–C** at different sizes; (d–f) SEM images of **Co^{3+}–N–C** at different sizes.

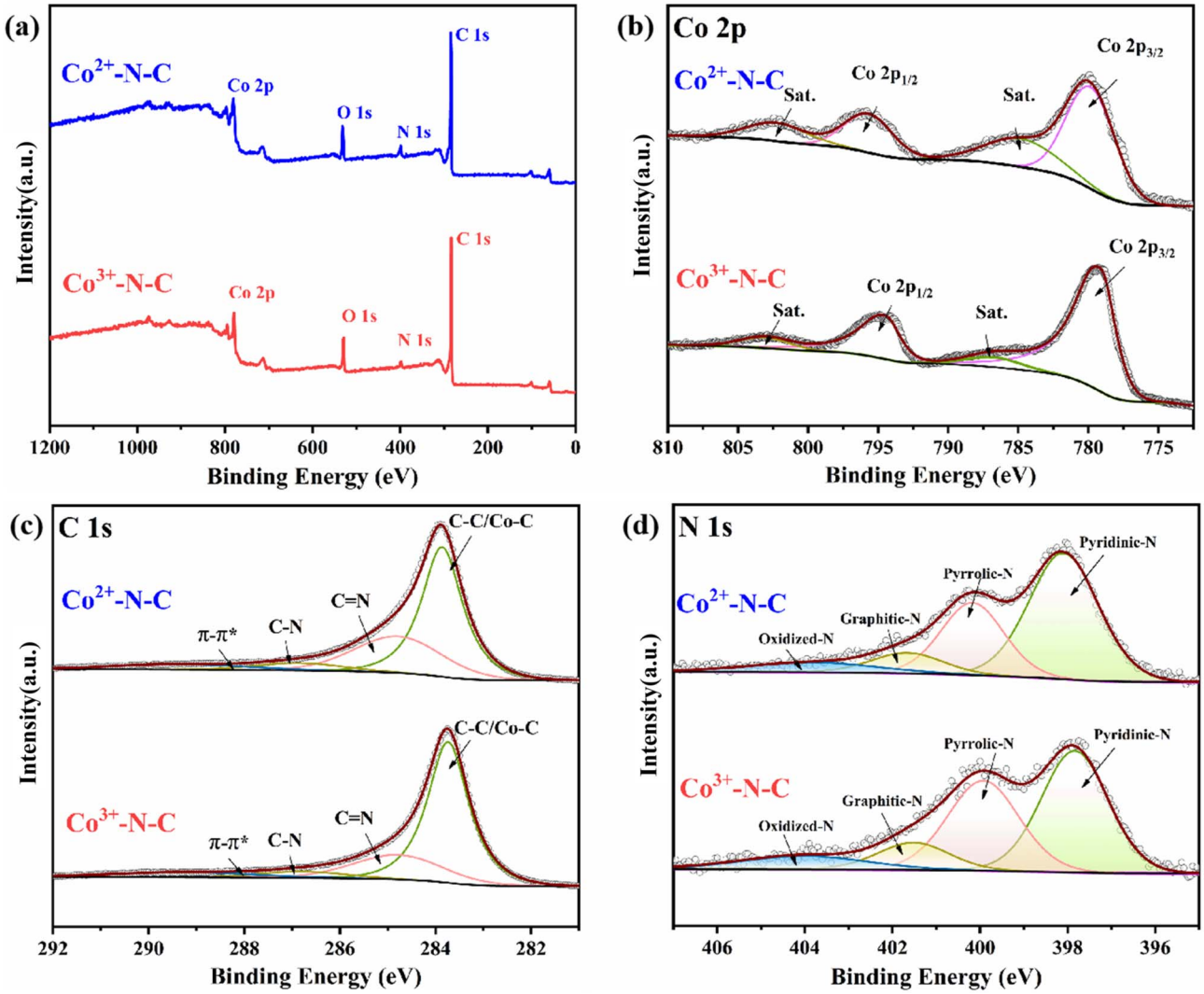

Fig. 4 $Co^{2+/3+}$–N–C catalysts: (a) XPS full spectrum; (b) high-resolution Co 2p spectrum; (c) high-resolution C 1s spectrum; (d) high-resolution N 1s spectrum.

a critical influence on the electronic structure of cobalt. Compared to Co^{3+} (with a $3d^6$ configuration), Co^{2+} possesses a $3d^7$ configuration, resulting in a higher number of d electrons. The higher initial d-electron density enhances the interaction between the Co^{2+} center and the electronegative N/C ligands, promoting greater delocalization of electron density towards the ligands. This intensified metal–ligand charge transfer effect consequently leads to a relatively weakened effective electron shielding at the Co^{2+} site under the final state probed by XPS, thereby increasing its core-electron binding energy.[46–49] This manifests as a shift of the Co 2p peaks for **Co^{2+}–N–C** to higher binding energies compared to those for **Co^{3+}–N–C**. Fig. 4c presents the C 1s spectra of the **Co^{2+}–N–C** and **Co^{3+}–N–C** catalysts. Distinct peaks corresponding to C–N and C=N bonds can be clearly observed, which strongly confirms the existence of nitrogen doping within the carbon matrix.[50] The relative proportions of different carbon species further reveal the structural characteristics, as summarized in Table S1. After the peak-fitting treatment of the N 1s signals shown in Fig. 4d, four characteristic peaks of nitrogen types located at 398.09 eV, 400.17 eV, 401.66 eV, and 403.81 eV are clearly presented. These peaks are attributed to pyridinic nitrogen, pyrrolic nitrogen, graphitic nitrogen, and oxidized nitrogen in sequence.[51] According to previous studies, within the catalyst system, the metal–nitrogen bonds constructed by pyridinic nitrogen have been widely recognized as highly efficient active sites in the ORR and OER processes.[52,53] Focusing on the **Co–N–C** samples we prepared (for specific relevant integral proportion data, see SI Table S2), the atomic content of pyridinic nitrogen in the **Co^{2+}–N–C** catalyst is 54.42%, and this catalyst contains the pyridinic nitrogen–Co structural unit. From the perspective of the coordination environment, the Co^{2+} ion has a $3d^7$ electronic structure, endowing it with certain electron-donating and electron-accepting capabilities. During the construction of the **Co^{2+}–N–C** system, the electron cloud density distribution around nitrogen atoms is mutually adapted to the electronic structure

of Co^{2+} ions, creating a coordination environment conducive to the formation of metal–nitrogen bonds. This apt environment promotes the interaction of Co^{2+} with nitrogen atoms and increases the number of metal–nitrogen bonds, which promises excellent electrocatalytic activity for **Co^{2+}–N–C** catalysts.[54]

Electrochemical performance analysis

ORR electrocatalytic activity. First, by means of the rotating disk electrode technique, the two synthesized catalysts, **Co^{2+}–N–C** and **Co^{3+}–N–C**, were respectively placed in an oxygen-saturated and a nitrogen-saturated 0.1 M KOH electrolyte environment. Cyclic voltammetry (CV) was used to conduct tests to evaluate the ORR performance of the two catalysts. The test results indicate that, in the oxygen-saturated electrolyte system, a significant cathodic peak can be clearly observed (see SI Fig. S4 for details). This phenomenon confirms that the two samples possess ORR activity.[55] Notably, the **Co^{2+}–N–C** oxygen electroreduction peak was more positive (0.77 V *vs.* RHE), indicating a superior electrocatalytic ORR activity. Subsequently, as shown in Fig. 5a, linear sweep voltammetry (LSV) curves were obtained under the conditions of a rotation rate of 1600 rpm and a scan rate of 5 mV s^{-1}. Among the tested catalysts, compared with **Co^{3+}–N–C**, **Co^{2+}–N–C** exhibits a higher onset potential (E_{onset} = 0.86 V *vs.* RHE) and half-wave potential ($E_{1/2}$ = 0.77 V *vs.* RHE), and its limiting current density is relatively large (3.6 mA cm^{-1}). Evidently, the ORR catalytic activity of **Co^{2+}–N–C** is superior to that of the **Co^{3+}–N–C** catalyst. Although **Co^{2+}–N–C** is slightly inferior to commercial Pt/C ($E_{1/2}$ = 0.83 V), when comparing its onset potential and half-wave potential with those of the **Co–N–C** ORR catalysts reported in recent literature (specific data are shown in Table S3), it is found that the catalytic activity of the **Co^{2+}–N–C** catalyst is comparable to that of most state-of-the-art transition-metal-based catalysts. To reveal the ORR kinetics, the Tafel slopes and kinetic current densities (J_k) of **Co^{2+}–N–C** and **Co^{3+}–N–C** were calculated (eqn (S3)). As can be seen from Fig. 5d, the Tafel slope value of **Co^{2+}–N–C** is 107.5 mV dec^{-1}, which is significantly lower than that of **Co^{3+}–N–C** (125.8 mV dec^{-1}). This indicates that the **Co^{2+}–N–C** catalyst has a faster reaction kinetics during the ORR process, which is undoubtedly more favorable for the efficient promotion of the electrochemical reaction.[56] At the same time, we also replaced the electrolyte solution with 0.1 M $HClO_4$ and 0.1 M K_2SO_4 for the test. From the variation of its measured LSV curve (Fig. 5b and c) and the corresponding Tafel slope (Fig. 5e and f), **Co^{2+}–N–C** also showed the same direction of the difference in performance, and still maintained the performance advantage over **Co^{3+}–N–C**. The kinetic current density was calculated according to the K–L equation (eqn (S4) and (S5)).[57] Under the test condition of 0.80 V, the kinetic current density J_k value of **Co^{2+}–N–C** was 3.21 mA cm^{-2}, which was larger than that of **Co^{3+}–N–C** (3.06 mA cm^{-2}). Generally speaking, in electrochemical reactions, the higher the onset potential and half-wave potential are, the larger the kinetic current density is, and the faster the kinetic rate of the corresponding reaction is.[58] To deeply investigate the ORR activities of **Co^{2+}–N–C** and **Co^{3+}–N–C**, this study systematically measured the LSV curves at rotation speeds ranging from 400 to 2025 rpm. The corresponding data are shown in Fig. 5g and S6. Based on the LSV curves, the number of electrons transferred during the ORR process was precisely calculated using eqn (S6) and (S7). The results demonstrate that at a potential of 0.4 V (*vs.* RHE), the electron transfer numbers for **Co^{2+}–N–C** and **Co^{3+}–N–C** are 3.32 and 3.08, respectively. This indicates that **Co^{2+}–N–C** catalyzes the oxygen reduction reaction more closely to the $4e^-$ transfer pathway,[59] implying that **Co^{2+}–N–C** catalysts are more inclined to the efficient reaction pathway for the direct reduction of oxygen to water, which in turn improves the energy conversion efficiency of the whole ORR process.

In this work, cyclic voltammetry (CV) was applied to measure the current response in the non-faradaic potential region (Fig. S7). The electrochemical double-layer capacitance (C_{dl}) was determined by further calculating the slope of the linear fit so as to visually assess the actual electrochemically active area (ECSA) of the catalysts in the catalytic process.[60] As can be seen from Fig. S5, the C_{dl} value of **Co^{2+}–N–C** (3.32 mF cm^{-2}) is higher than that of **Co^{3+}–N–C** (2.38 mF cm^{-2}). Given that the slope of the C_{dl} is directly proportional to the actual ECSA, it means that under the same conditions, **Co^{2+}–N–C** has a larger electrochemically active surface area and exposes relatively more active sites on its surface. These active sites are regulated by the metal valence state centers. Therefore, compared with **Co^{3+}–N–C**, the metal valence state centers of **Co^{2+}–N–C** are more favorable for the catalysis of the ORR, thus exhibiting higher catalytic activity. Fig. 5h shows the results of the electrochemical impedance spectroscopy (EIS) tests for the two catalysts. Obviously, the Nyquist plot of **Co^{2+}–N–C** exhibits a narrower semi-circular arc, which intuitively indicates that it has a lower resistivity.[61] Judging from the specific data, the resistance value of **Co^{2+}–N–C** is 2.3 Ω, which is lower than the 4.6 Ω of **Co^{3+}–N–C**. The low-resistance characteristic enables **Co^{2+}–N–C** to conduct electrons rapidly, thereby effectively improving the electrocatalytic efficiency and demonstrating significant advantages in terms of kinetics. Stability is a key indicator of catalyst performance, for which the electrochemical stability of two **Co–N–C** materials was further tested. As can be seen from Fig. 5i, under the constant-voltage test in a 0.1 M KOH electrolyte solution, both of them performed well. **Co^{2+}–N–C** could still maintain approximately 91.3% of the initial current after 252 hours, and **Co^{2+}–N–C** could also maintain about 90.3% of the initial current after the same period. This indicates that this type of **Co–N–C** material has good electrocatalytic stability in a harsh electrolyte environment.

OER electrocatalytic activity. In the exploration of the ORR performance of **Co^{2+}–N–C** and **Co^{3+}–N–C** materials, it has been found that the **Co^{2+}–N–C** material exhibits better performance. Considering the relevance of oxygen electrode reactions and the potential influence of the materials' own characteristics on different reactions, next, we will focus on the research of the OER performance of these two materials. To accurately evaluate the OER catalytic performance of the synthesized **Co–N–C** materials, 0.1 M and 1.0 M KOH electrolyte solutions were selected to set up a three-electrode system: the working electrodes were modified with the prepared **Co^{2+}–N–C** and **Co^{3+}–N–**

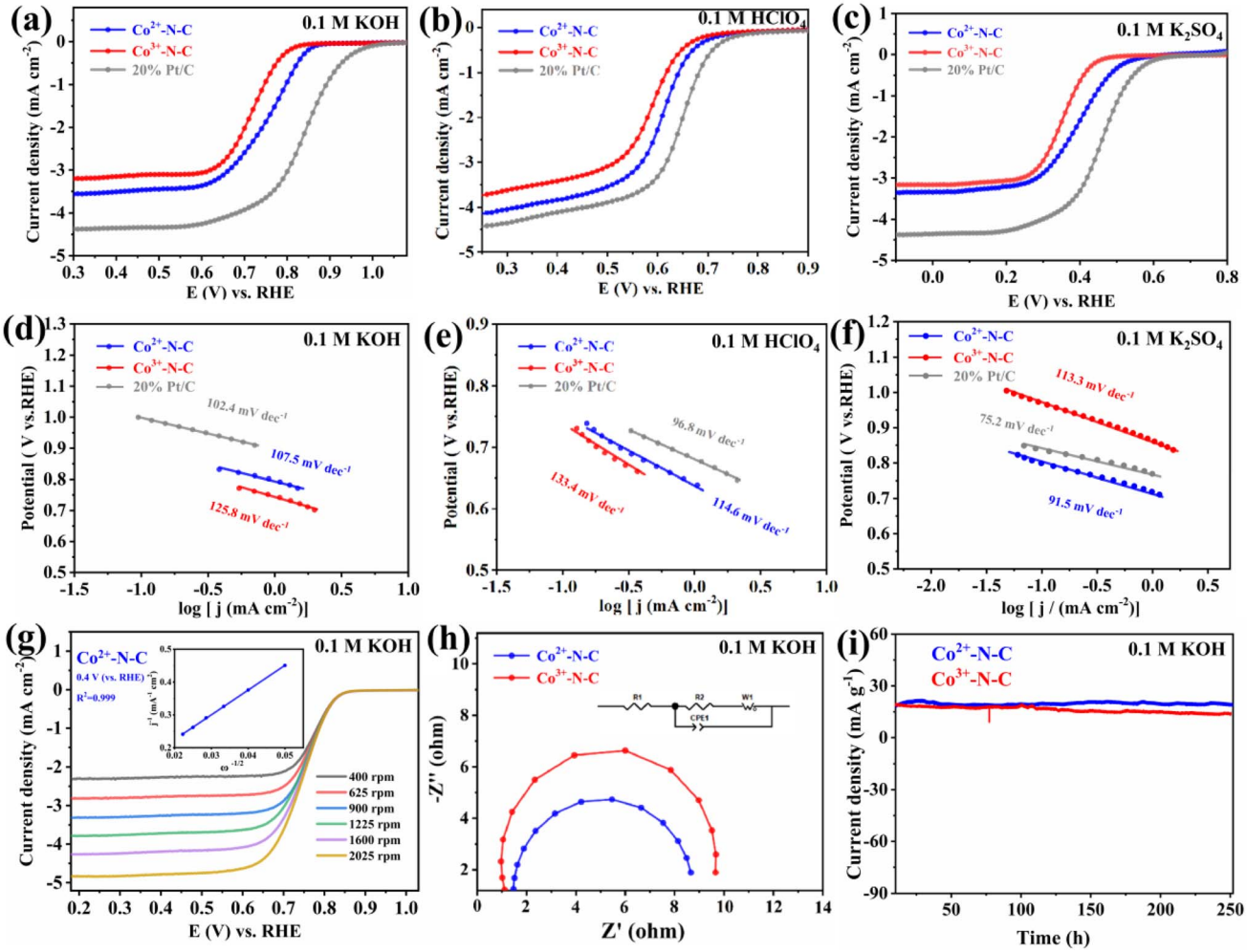

Fig. 5 ORR performance diagrams of two **Co–N–C** catalysts in different electrolytes: (a) LSV curves in an alkaline electrolyte (0.1 M KOH); (b) LSV curves in an acidic electrolyte (0.1 M $HClO_4$); (c) LSV curves in a neutral electrolyte (0.1 M K_2SO_4); (d) Tafel slopes in a 0.1 M KOH electrolyte; (e) Tafel slopes in a 0.1 M $HClO_4$ electrolyte; (f) Tafel slopes in a 0.1 M K_2SO_4 electrolyte; (g) LSV curves and K–L illustrations of **Co^{2+}–N–C** at 400–2025 rpm in a 0.1 M KOH electrolyte; (h) EIS diagrams in a 0.1 M KOH electrolyte; (i) *i*–*t* graphs in a 0.1 M KOH electrolyte.

C materials, while the reference electrode was an RHE and the counter electrode was a carbon rod. By measuring the current density at different potentials, polarization curves were plotted. Then, key parameters such as the OER onset potential, overpotential, and Tafel slope of the materials were obtained to conduct an in-depth exploration of their catalytic activity and kinetic characteristics under different electrolyte concentrations.

According to the LSV curves in Fig. 6a and d, in the two electrolyte solution environments shown, it can be clearly seen that the catalytic performance of the two **Co–N–C** catalysts is indeed slightly inferior to that of the commercial IrO_2 catalyst. However, it is worth noting that among these two **Co–N–C** catalysts, the OER catalytic efficiency of **Co^{2+}–N–C** is always superior to that of **Co^{3+}–N–C**. Judging from the trend of the curves, at each potential, the current density of **Co^{2+}–N–C** is greater than that of **Co^{3+}–N–C**. This indicates that **Co^{2+}–N–C** can more effectively promote electron transfer and the progress of the reaction during the OER process, thus having relatively higher catalytic activity.[62] This performance difference may stem from the different electronic structures and coordination environments of Co^{2+} and Co^{3+}, which result in different interactions between them and the N–C support, as well as different adsorption and desorption abilities for OER reaction intermediates. Fig. 6b and e shows that regardless of the concentration, the overpotential of **Co^{2+}–N–C** is always lower than that of **Co^{3+}–N–C**. This indicates that the **Co^{2+}–N–C** catalyst needs to overcome a relatively smaller energy barrier during the electrochemical reaction, suggesting that its catalytic performance is relatively better and the reaction can proceed more easily. From the perspective of OER kinetics, in a 0.1 M KOH electrolyte solution environment, the Tafel slopes of **Co^{2+}–N–C** and **Co^{3+}–N–C** were calculated (as shown in Fig. S8a). Among them, the Tafel value of **Co^{2+}–N–C** is 130.5 mV dec^{-1}, which is significantly lower than that of **Co^{3+}–N–C** (139.0 mV dec^{-1}). This result strongly indicates that the **Co^{2+}–N–C** catalyst exhibits faster reaction kinetics during the corresponding reaction process, which is more favorable for the rapid progress of the

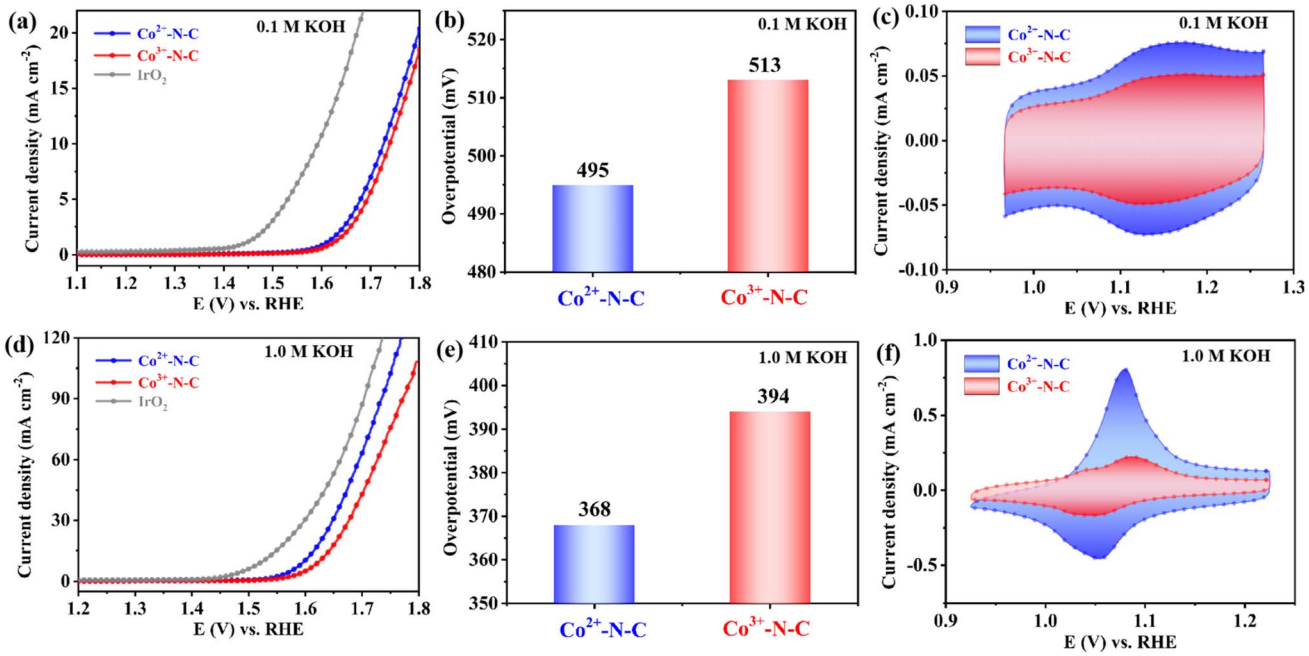

Fig. 6 OER characterization of Co–N–C with different valence states and commercial IrO_2 in 0.1 M and 1.0 M KOH: (a–c) 0.1 M KOH: LSV curves, overpotential at 10 mA cm^{-2}, and Co oxidation CV curves; (d–f) 1.0 M KOH: LSV curves, overpotential at 10 mA cm^{-2}, and Co oxidation CV curves.

electrochemical reaction. It is worth mentioning that the same conclusion about the Tafel slope was obtained in the 1.0 M KOH electrolyte system (as shown in Fig. S8b).[63]

As can be clearly seen from the CV curves shown in Fig. S9, in the two electrolyte solution systems of 0.1 M KOH and 1.0 M KOH, the redox peak positions of the two **Co–N–C** materials fall within the ranges of 0.916–1.216 V and 0.926–1.226 V, respectively. A more in-depth analysis of the CV curves within these two narrower potential intervals (as shown in Fig. 6c and f) shows that the **Co–N–C** materials centered on different metal valence states exhibit different electrochemical active areas. According to the attached eqn (S8), the integral operation was performed for the charges in the intervals corresponding to the highest voltage peaks (*i.e.*, the oxidation peaks, located near 1.16 V and 1.108 V, respectively) (see Table S5 for details). The calculations showed that the electrochemically active surface area of **Co^{2+}–N–C** significantly surpassed that of **Co^{3+}–N–C**. This result clearly indicates that in the catalytic process of the OER, the catalytic sites where Co^{2+} is located have better activity, which in turn enables **Co^{2+}–N–C** to exhibit better performance in this catalytic process.[64] In addition, it can also be clearly observed from the figure that within different potential ranges, the changing trends of the current densities of the two types of materials also differ. This is most likely due to the differences in their electronic structures and surface properties, which further reveals the crucial influence of the metal valence states on the catalytic performance of the materials. According to Fig. S5 and S10, in the two different electrolyte solution systems, the C_{dl} value of **Co^{2+}–N–C** is significantly larger, which further verifies that it has a larger electrochemically active area.

HER electrocatalytic activity. To investigate the HER catalytic performance of **Co–N–C** materials with different metal valence states at the center, a three-electrode system was used at room temperature. The tests were conducted using 0.5 M H_2SO_4 (acidic), 0.1 M K_2SO_4 (neutral), and 0.1 M KOH (alkaline) as electrolytes, respectively. Using 20 wt% commercial Pt/C as the benchmark, all potentials were referenced to the RHE, with a scan rate of 5 mV s^{-1}. From the LSV curve test results in Fig. 7a–c, it can be seen that under different electrolyte solution conditions such as acidic, neutral, and alkaline conditions, the catalytic performance of **Co^{2+}–N–C** is superior to that of **Co^{3+}–N–C**. Meanwhile, according to the overpotential comparison chart in Fig. S11, in the acidic medium, when the current density reaches 10 mA cm^{-2}, the corresponding overpotential of **Co^{2+}–N–C** is 412 mV. To more comprehensively analyze the HER kinetic characteristics, we performed a fitting operation on the Tafel plots according to the attached eqn (S3). The obtained results are shown in Fig. 7d and S12. Taking the 0.5 M H_2SO_4 electrolyte solution as an example, the slope of **Co^{2+}–N–C** was determined to be 170.9 mV dec^{-1} through calculation. This value is significantly larger compared with that of the commercial 20% Pt/C (35.01 mV dec^{-1}), but slightly smaller than that of **Co^{3+}–N–C** (178.5 mV dec^{-1}). Nonetheless, **Co^{2+}–N–C** exhibits superior electrocatalytic performance to **Co^{3+}–N–C**. This phenomenon strongly implies that the catalytic active centers of **Co^{2+}–N–C** significantly promote the Volmer–Heyrovsky kinetic mechanism.[65] The results of the C_{dl} values shown in Fig. 7e and S5, S7, S13, S14 collectively indicate that **Co^{2+}–N–C** possesses more electrocatalytic active sites and thus exhibits superior HER electrocatalytic performance. To thoroughly investigate the stability of the two synthesized **Co–N–C** catalysts

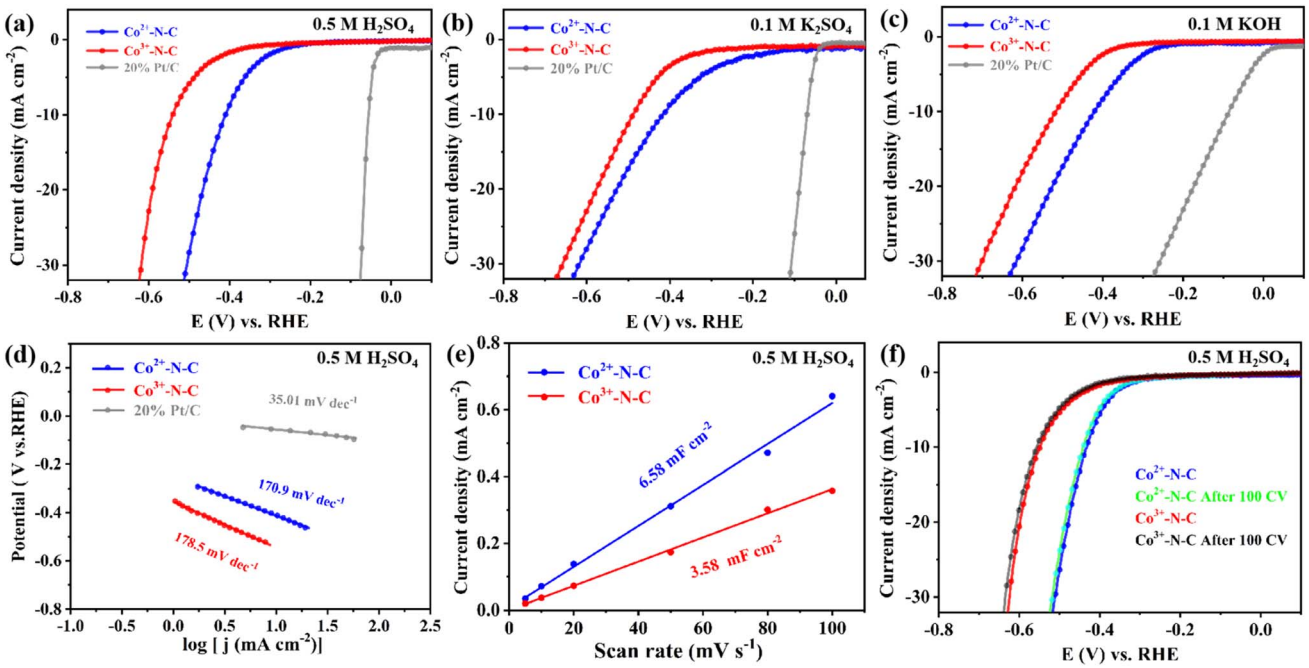

Fig. 7 HER performance curves of Co–N–C materials with two metal valence states and commercial 20% Pt/C materials in different electrolytes: (a) LSV curves in an acidic electrolyte (0.5 M H_2SO_4); (b) LSV curves in a neutral electrolyte (0.1 M K_2SO_4); (c) LSV curves in an alkaline electrolyte (0.1 M KOH); (d) Tafel slopes in a 0.5 M H_2SO_4 electrolyte; (e) double-layer capacitances (C_{dl}) in a 0.5 M H_2SO_4 electrolyte; (f) comparison diagrams of LSV curves before and after catalysis in a 0.5 M H_2SO_4 electrolyte.

under acidic conditions, catalytic reaction tests were conducted in a 0.5 M H_2SO_4 electrolyte solution respectively. The comparison of the corresponding curves before and after the reaction is shown in Fig. 7f. From this figure, it can be seen that the LSV curves of the two **Co–N–C** materials before and after catalysis basically overlap. That is, there is almost no change in their potentials, which further confirms that the materials possess more stable electrochemical performance in acidic electrolyte solutions.

Density functional theory (DFT) calculations

Although valence state modulation is a critical strategy for optimizing the electronic structure and catalytic performance of M–N–C catalysts, previous studies have primarily focused on Fe-based systems. For instance, research on the CO_2 reduction reaction (CO_2RR) has revealed intrinsic activity differences between Fe^{3+} and Fe^{2+} sites (*e.g.*, pyrrolic $Fe^{III}N_4$ *vs.* pyridinic $Fe^{II}N_4$).[26,66] Inspired by these findings, and to elucidate the influence of cobalt valence states on the selectivity across various electrocatalytic reactions, we adopted the structural classification from ref. 67 Using pyridinic Co^{2+}–N_4 and pyrrolic Co^{3+}–N_4 as computational models (Fig. 8a and b), DFT calculations were performed to probe the energy profiles of the reactions. The results demonstrate that the Co^{2+} sites simultaneously optimize the adsorption free energies of multiple key intermediates (O*, OH*, OOH* and H*) involved in ORR, OER, and HER, thereby significantly lowering the overpotentials of each reaction and endowing the material with superior trifunctional electrocatalytic activity. Carbon vacancies were introduced to maintain charge neutrality and structural stability of the Co^{3+} coordination environment, rather than to intentionally create additional active sites. To examine whether carbon vacancies could serve as potential reaction centers, we explicitly evaluated O_2 adsorption at the carbon vacancy sites. Further detailed descriptions can be found in Fig. S15 and S16 of the SI.

The Co^{2+} valence state endows the active centers (**Co–N–C**) with a distinct electronic configuration. Compared to higher-valence Co^{3+}, Co^{2+} possesses more d-electrons, resulting in a density of states near the Fermi level that is more favorable for forming neither too strong nor too weak "moderate adsorption" with key reaction intermediates (O*, OH*, OOH* and H*).[68] For both ORR and OER, the catalyst simultaneously reduces the Gibbs free energy of the key intermediates O*, OH* and OOH* (Fig. 8c and d), preventing any single step from becoming an insurmountable energy barrier and thereby facilitating a more efficient four-electron transfer pathway. Specifically, during the ORR process, the Gibbs free energy change (ΔG) for **Co^{2+}–N–C** is (−0.56 eV), which is lower than that of **Co^{3+}–N–C** (−0.40 eV). Similarly, for the OER process, the ΔG value of **Co^{2+}–N–C** is 1.72 eV, also lower than that of **Co^{3+}–N–C** (1.88 eV). For the HER, the hydrogen adsorption free energy (ΔG_{H^*}) serves as a descriptor for the rate-determining step, with an ideal value approaching 0 eV. The ΔG_{H^*} value of **Co^{2+}–N–C** (−0.04 eV) lies nearly perfectly at the apex of the volcano plot (Fig. 8e), indicating that the adsorption/desorption process of H* approaches thermodynamic equilibrium with a minimal kinetic barrier. This performance is markedly superior to that of **Co^{3+}–N–C**

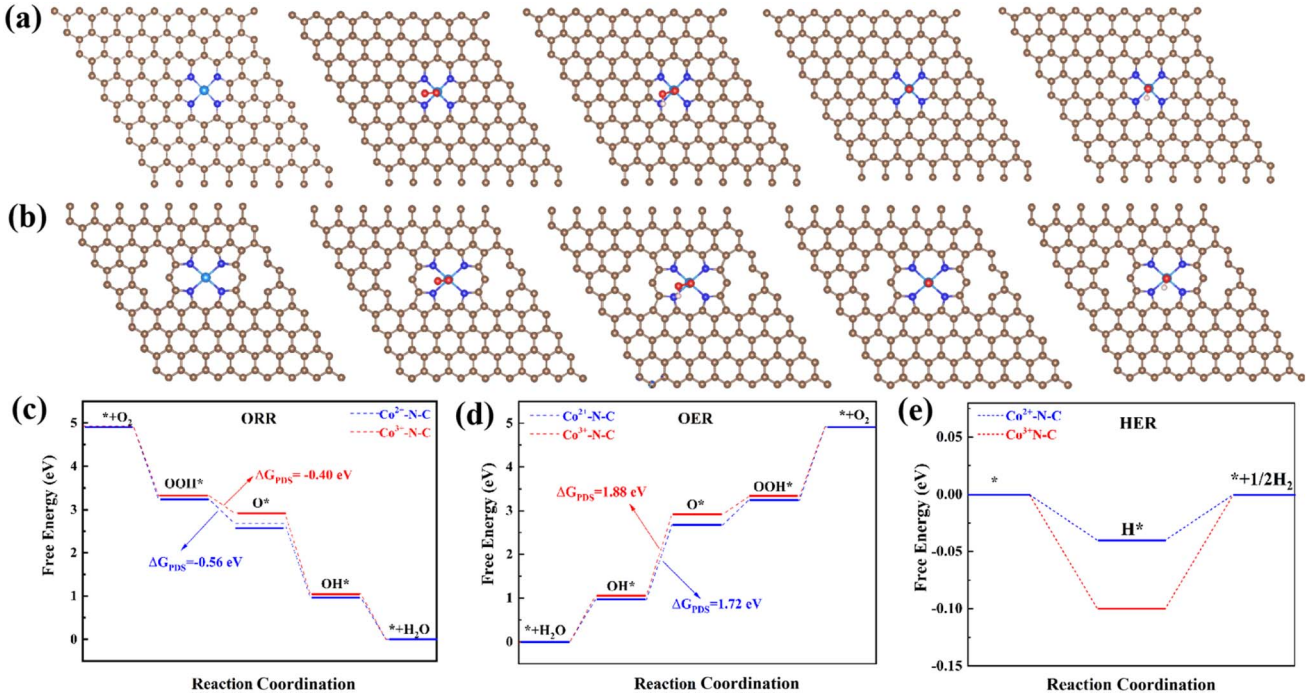

Fig. 8 (a) ORR reaction configurations on Co sites in Co^{2+}–N–C. (b) ORR reaction configurations on Co sites in Co^{3+}–N–C. (c–e) Free energy diagrams for ORR, OER, and HER pathways on $Co^{2+/3+}$–N–C catalysts.

(−0.10 eV), and thus exhibits weaker H* adsorption. We have performed additional electronic structure analyses, including partial density of states (PDOS) calculations, to further elucidate the origin of the different adsorption behaviors between Co^{2+} and Co^{3+} sites (detailed description can be found in Fig. S17 of the SI).

Conclusion

In summary, this work employed a rational coordination structure design strategy to select a system featuring a Co–N_6 coordination structure. Through precise modulation of the metal valence state, two MOFs with distinct metal valence states were successfully constructed. Using these MOFs as precursors, a pyrolysis process under a N_2 atmosphere was implemented, facilitating the transformation from the conventional Co–N_6 configuration into **Co–N–C** materials. This approach yielded final catalysts with similar overall architectures but distinct metal valence states, namely **Co^{2+}–N–C** and **Co^{3+}–N–C**. Electrochemical performance was systematically evaluated for **Co–N–C** materials with different metal valence states. The results demonstrate that, across various electrolyte solutions, the **Co^{2+}–N–C** catalyst exhibits significantly enhanced catalytic activity for the ORR, OER, and HER compared to the **Co^{3+}–N–C** catalyst. It is particularly noteworthy that in 0.1 M KOH electrolyte, the **Co^{2+}–N–C** catalyst retained 91.3% of its initial electrocatalytic performance after 252 h of continuous operation at an applied potential of 1.616 V (*vs.* RHE). This design not only facilitates an in-depth analysis of the performance differences among various catalysts but also strongly confirms that catalysts with metal centers of different valence states exhibit significant disparities in their electrocatalytic performance. This work proposes an innovative research approach for exploring the intrinsic relationship between metal valence states and electrocatalytic performance, which is expected to provide valuable references for the further development of this field.

Conflicts of interest

The authors declare no competing financial interest.

Data availability

The data that support the findings of this study are available from the corresponding author upon reasonable request.

Supplementary information (SI): the content comprehensively covers electrochemical calculations, density functional theory (DFT) calculations, PXRD patterns, TGA curves, LSV curves, overpotential data, CV curves, Tafel slope calculations, proportional analysis tables of integrated areas, and comparison tables benchmarking the electrocatalytic performance of this study against previously reported catalysts of the same type. See DOI: https://doi.org/10.1039/d6ra00087h.

Acknowledgements

This research was supported by Zhejiang Provincial Natural Science Foundation of China under Grant No. LY24B010001, the National Natural Science Foundation of China under Grant

No. 22478152, the Qin Shen Scholar Program of Jiaxing University (CD70623027).

References

1 L. Quan, H. Jiang, G. Mei, Y. Sun and B. You, Bifunctional Electrocatalysts for Overall and Hybrid Water Splitting, *Chem. Rev.*, 2024, **124**, 3694–3812.

2 K.-M. Zhao, D.-X. Wu, W.-K. Wu, J.-B. Nie, F.-S. Geng, G. Li, H.-Y. Shi, S.-C. Huang, H. Huang, J. Zhang, Z.-Y. Zhou, Y.-C. Wang and S.-G. Sun, Identifying high-spin hydroxyl-coordinated $Fe^{3+}N_4$ as the active centre for acidic oxygen reduction using molecular model catalysts, *Nat. Catal.*, 2025, **8**, 422–435.

3 K. Yue, R. Lu, M. Gao, F. Song, Y. Dai, C. Xia, B. Mei, H. Dong, R. Qi, D. Zhang, J. Zhang, Z. Wang, F. Huang, B. Y. Xia and Y. Yan, Polyoxometalated metal-organic framework superstructure for stable water oxidation, *Science*, 2025, **388**, 430–436.

4 J. Yang, H. Xu, J. Li, K. Gong, F. Yue, X. Han, K. Wu, P. Shao, Q. Fu, Y. Zhu, W. Xu, X. Huang, J. Xie, F. Wang, W. Yang, T. Zhang, Z. Xu, X. Feng and B. Wang, Oxygen- and proton-transporting open framework ionomer for medium-temperature fuel cells, *Science*, 2024, **385**, 1115–1120.

5 N. Sun, S. S. A. Shah, Z. Lin, Y.-Z. Zheng, L. Jiao and H.-L. Jiang, MOF-based electrocatalysts: An overview from the perspective of structural design, *Chem. Rev.*, 2025, **125**, 2703–2792.

6 W. W. Tian, J. T. Ren, H. Y. Wang, L. Wang and Z. Y. Yuan, Bioinspired binary-site catalysts for novel urea-assisted Zn-air battery: A transfer station between renewable energy and hydrogen, *Appl. Catal. B Environ. Energy*, 2024, **354**, 124115.

7 W. Shi, T. Shen, C. Xing, K. Sun, Q. Yan, W. Niu, X. Yang, J. Li, C. Wei, R. Wang, S. Fu, Y. Yang, L. Xue, J. Chen, S. Cui, X. Hu, K. Xie, X. Xu, S. Duan, Y. Xu and B. Zhang, Ultrastable supported oxygen evolution electrocatalyst formed by ripening-induced embedding, *Science*, 2025, **387**, 791–796.

8 J. Zhao, Y. Guo, Z. Zhang, X. Zhang, Q. Ji, H. Zhang, Z. Song, D. Liu, J. Zeng, C. Chuang, E. Zhang, Y. Wang, G. Hu, M. A. Mushtaq, W. Raza, X. Cai and F. Ciucci, Out-of-plane coordination of iridium single atoms with organic molecules and cobalt–iron hydroxides to boost oxygen evolution reaction, *Nat. Nanotechnol.*, 2025, **20**, 57–66.

9 Y. Ding, F. Zhang, X. Cao, Y. Guo, L. Sun and B. Zhang, Reserved charges in a long-lived NiOOH phase drive catalytic water oxidation, *Nat. Chem.*, 2026, **18**, 120–127.

10 A. Li, S. Kong, K. Adachi, H. Ooka, K. Fushimi, Q. Jiang, H. Ofuchi, S. Hamamoto, M. Oura, K. Higashi, T. Kaneko, T. Uruga, N. Kawamura, D. Hashizume and R. Nakamura, Atomically dispersed hexavalent iridium oxide from MnO_2 reduction for oxygen evolution catalysis, *Science*, 2024, **384**, 666–670.

11 B. Zhang, J. Wang, G. Liu, C. M. Weiss, D. Liu, Y. Chen, L. Xia, P. Zhou, M. Gao, Y. Liu, J. Chen, Y. Yan, M. Shao, H. Pan and W. Sun, A strongly coupled Ru–CrOx cluster–cluster heterostructure for efficient alkaline hydrogen electrocatalysis, *Nat. Catal.*, 2024, **7**, 441–451.

12 C.-Y. Wang, C.-Z. Ren, K.-M. Fang, J.-J. Feng, Y. C. Shi, Y.-J. Gao and A.-J. Wang, Synergistic catalysis of satellite single-atomic Fe sites and RuFe nanoclusters on N-rich carbon nanoflowers for boosting oxygen reduction, *J. Colloid Interface Sci.*, 2025, **699**, 138169, DOI: 10.1016/j.jcis.2025.138169.

13 Y. Zhao, J. Wan, C. Ling, Y. Wang, H. He, N. Yang, R. Wen, Q. Zhang, L. Gu, B. Yang, Z. Xiang, C. Chen, J. Wang, X. Wang, Y. Wang, H. Tao, X. Li, B. Liu, S. Zhang and D. Wang, Acidic oxygen reduction by single-atom Fe catalysts on curved supports, *Nature*, 2025, **644**, 668–675.

14 K. Y. Zhao, M. C. Luo, Y. F. Zhang, X. X. Chang and B. J. Xu, Coupled cation–electron transfer at the Pt(III)/perfluorosulfonic acid ionomer interface and its impact on the oxygen reduction reaction kinetics, *Nat. Catal.*, 2025, **8**, 46–57.

15 H. Li, R. Zeng, Z. Shi, H. Wang, D. Leshchev, E. Stavitski, M. M. T. Cruz, W. Xu, M.-J. Kim, A. M. Villarino, Q. Li, D. A. Muller and H. D. Abruña, Rational design of high-performance low-loading oxygen reduction catalysts for alkaline fuel cells, *Nat. Mater.*, 2026, **25**, DOI: 10.1038/s41563-025-02422-4.

16 J. Zhang, X. Fu, S. Kwon, K. Chen, X. Liu, J. Yang, H. Sun, Y. Wang, T. Uchiyama, Y. Uchimoto, S. Li, Y. Li, X. Fan, G. Chen, F. Xia, J. Wu, Y. Li, Q. Yue, L. Qiao, D. Su, H. Zhou, W. A. Goddard and Y. Kang, Tantalum-stabilized ruthenium oxide electrocatalysts for industrial water electrolysis, *Science*, 2025, **387**, 48–55.

17 L. Magnier, G. Cossard, V. Martin, C. Pascal, V. Roche, E. Sibert, I. Shchedrina, R. Bousquet, V. Parry and M. Chatenet, Fe–Ni-based alloys as highly active and low-cost oxygen evolution reaction catalyst in alkaline media, *Nat. Mater.*, 2024, **23**, 252–261.

18 Z. Li, Y. Wang, H. Liu, Y. Feng, X. Du, Z. Xie, J. Zhou, Y. Liu, Y. Song, F. Wang, M. Sui, Y. Lu, F. Fang and D. Sun, Electroreduction-driven distorted nanotwins activate pure Cu for efficient hydrogen evolution, *Nat. Mater.*, 2025, **24**, 424–432.

19 Y. Bai, K. Li, N. Han, J. Kim, R. Zhang, S. Mahesh, A. S. Zeraati, B. R. Sutherland, K. Chow, Y. Liang, S. Hoogland, J. E. Huang, D. Sinton, E. H. Sargent and J. H. Simpers, Earth-abundant electrocatalysts for acidic oxygen evolution, *Nat. Catal.*, 2026, **9**, 28–36.

20 A. A. Feidenhans'l, Y. N. Regmi, C. Wei, D. Xia, J. Kibsgaard and L. A. King, Precious Metal Free Hydrogen Evolution Catalyst Design and Application, *Chem. Rev.*, 2024, **124**, 5617–5667.

21 Z. Levell, J. Le, S. Yu, R. Wang, S. Ethirajan, R. Rana, A. Kulkarni, J. Resasco, D. Lu, J. Cheng and Y. Liu, Emerging Atomistic Modeling Methods for Heterogeneous Electrocatalysis, *Chem. Rev.*, 2024, **124**, 8620–8656.

22 Y. Zhao, D. P. A. Saseendran, C. Huang, C. A. Triana, W. R. Marks, H. Chen, H. Zhao and G. R. Patzke, Oxygen Evolution/Reduction Reaction Catalysts: From *In Situ*

Monitoring and Reaction Mechanisms to Rational Design, *Chem. Rev.*, 2023, **123**, 6257–6358.

23 C. Xie, W. Chen, Y. Wang, Y. Yang and S. Wang, Dynamic evolution processes in electrocatalysis: structure evolution, characterization and regulation, *Chem. Soc. Rev.*, 2024, **53**, 10852–10877.

24 H. Y. Wang, S. F. Hung, H. Y. Chen, T. S. Chan, H. M. Chen and B. Liu, Operando Identification of Geometrical-Site-Dependent Water Oxidation Activity of Spinel Co_3O_4, *J. Am. Chem. Soc.*, 2016, **138**, 36–39.

25 Y. Bi, Z. Cai, D. Zhou, Y. Tian, Q. Zhang, Q. Zhang, Y. Kuang, Y. Li, X. Sun and X. Duan, Understanding the incorporating effect of Co^{2+}/Co^{3+} in NiFe-layered double hydroxide for electrocatalytic oxygen evolution reaction, *J. Catal.*, 2018, **358**, 100–107.

26 J. Gu, C.-S. Hsu, L. Bai, H. M. Chen and X. Hu, Atomically dispersed Fe^{3+} sites catalyze efficient CO_2 electroreduction to CO, *Science*, 2019, **364**, 1091–1094.

27 K. Sun, J. Dong, H. Sun, X. Wang, J. Fang, Z. Zhuang, S. Tian and X. Sun, $Co(CN)_3$ catalysts with well-defined coordination structure for the oxygen reduction reaction, *Nat. Catal.*, 2023, **6**, 1164–1173.

28 H. Xu, D. Cheng, D. Cao and X. C. Zeng, Revisiting the universal principle for the rational design of single-atom electrocatalysts, *Nat. Catal.*, 2024, **7**, 207–218.

29 Z. Y. Wu, M. X. Chen, S. Q. Chu, Y. Lin, H. W. Liang, J. Zhang and S. H. Yu, Switching Co/N/C Catalysts for Heterogeneous Catalysis and Electrocatalysis by Controllable Pyrolysis of Cobalt Porphyrin, *iScience*, 2019, **15**, 282–290.

30 H. Yin, Y. Dou, S. Chen, Z. Zhu, P. Liu and H. Zhao, 2D Electrocatalysts for Converting Earth-Abundant Simple Molecules into Value-Added Commodity Chemicals: Recent Progress and Perspectives, *Adv. Mater.*, 2019, **32**, 1904870.

31 W. Liu, Q. Ru, S. Zuo, S. Yang, J. Han and C. Yao, Controllable synthesis of nitrogen-doped carbon nanotubes derived from halloysite-templated polyaniline towards nonprecious ORR catalysts, *Appl. Surf. Sci.*, 2019, **469**, 269–275.

32 X. Chia and M. Pumera, Characteristics and performance of two-dimensional materials for electrocatalysis, *Nat. Catal.*, 2018, **1**, 909–921.

33 M. I. H. Mohideen, C. Lei, J. Tuček, O. Malina, F. Brivio, V. Kasneryk, Z. Huang, M. Mazur, X. Zou, P. Nachtigall, J. Čejka and R. E. Morris, Magneto-structural correlations of novel kagomé-type metal organic frameworks, *J. Mater. Chem. C*, 2019, **7**, 8034–8044.

34 J. M. Lin, B. S. Huang, Y. F. Guan, Z. Q. Liu, D. Y. Wang and W. Dong, Syntheses, structures and properties of seven H_2BTA coordinating 3-D metallic complexes containing 0-, 1-, 2-, and 3-D frameworks (H_2BTA = bis(tetrazolyl)amine), *CrystEngComm*, 2009, **11**, 349–358.

35 X. Xie, C. He, B. Li, Y. He, D. A. Cullen, E. C. Wegener, A. J. Kropf, U. Martinez, Y. Cheng, M. H. Engelhard, M. E. Bowden, M. Song, T. Lemmon, X. S. Li, Z. Nie, J. Liu, D. J. Myers, P. Zelenay, G. Wang, G. Wu, V. Ramani and Y. Shao, Performance enhancement and degradation mechanism identification of a single-atom Co–N–C catalyst for proton exchange membrane fuel cells, *Nat. Catal.*, 2020, **3**, 1044–1054.

36 J. W. Chang, W. Jing, X. Yong, A. Cao, J. K. Yu, H. Wu, C. Z. Wan, S. Y. Wang, G. I. N. Waterhouse, B. Yang, Z. Y. Tang, X. F. Duan and S. Y. Lu, Synthesis of ultrahigh-metal-density single-atom catalysts via metal sulfide-mediated atomic trapping, *Nat. Synth.*, 2024, **3**, 1427–1438.

37 T. H. Hsieh, Y. Z. Wang and K. S. Ho, Cobalt-Based Cathode Catalysts for Oxygen-Reduction Reaction in an Anion Exchange Membrane Fuel Cell, *Membranes*, 2022, **12**, 699.

38 Y. Cheng, S. Liu, J. Jiao, M. Zhou, Y. Wang, X. Xing, Z. Chen, X. Sun, Q. Zhu, Q. Qian, C. Wang, H. Liu, Z. Liu, X. Kang and B. Han, Highly Efficient Electrosynthesis of Glycine over an Atomically Dispersed Iron Catalyst, *J. Am. Chem. Soc.*, 2024, **146**, 10084–10092.

39 W. Zhang, X. Yao, S. Zhou, X. Li, L. Li, Z. Yu and L. Gu, ZIF-8/ZIF-67-Derived Co-N_x-Embedded 1D Porous Carbon Nanofibers with Graphitic Carbon-Encased Co Nanoparticles as an Efficient Bifunctional Electrocatalyst, *Small*, 2018, **14**, 1800423.

40 H. Liu, S. Yi, Y. Wu, H. Wu, J. Zhou, W. Liang, J. Cai and H. Xu, An efficient Co-N/C electrocatalyst for oxygen reduction facilely prepared by tuning cobalt species content, *Int. J. Hydrogen Energy*, 2020, **45**, 16105–16113.

41 X. Wang, J. Zhang, D. Ma, X. Feng, L. Wang and B. Wang, Metal-Organic Framework-Derived Trimetallic Nanocomposites as Efficient Bifunctional Oxygen Catalysts for Zinc-Air Batteries, *ACS Appl. Mater. Interfaces*, 2021, **13**, 33209–33217.

42 J. Zhang, Y. Wu, L. Zhang and W. Gao, Graphitic N-Rich Graphene for Nonradical Peroxymonosulfate Activation, *ACS Appl. Nano Mater.*, 2024, **7**, 13134–13141.

43 J. Li, T. Lu, Y. Fang, G. Zhou, M. Zhang, H. Pang, J. Yang, Y. Tang and L. Xu, The manipulation of rectifying contact of Co and nitrogen-doped carbon hierarchical superstructures toward high-performance oxygen reduction reaction, *Carbon Energy*, 2024, **6**, e529.

44 Y. C. Huang, K. S. Ho and H. T. Lee, Calcined cobalt-chelated, N-containing poly(methylenediphenyl urea) as an ORR cathode catalyst, *React. Funct. Polym.*, 2023, **192**, 105718.

45 E. S. Andreiadis, P.-A. Jacques, P. D. Tran, A. Leyris, M. Chavarot-Kerlidou, B. Jousselme, M. Matheron, J. Pécaut, S. Palacin, M. Fontecave and V. Artero, Molecular engineering of a cobalt-based electrocatalytic nanomaterial for H_2 evolution under fully aqueous conditions, *Nat. Chem.*, 2013, **5**, 48–53.

46 M. C. Biesinger, B. P. Payne, A. P. Grosvenor, L. W. M. Lau, A. R. Gerson and R. St. C. Smart, Resolving surface chemical states in XPS analysis of first row transition metals, oxides and hydroxides: Cr, Mn, Fe, Co and Ni, *Appl. Surf. Sci.*, 2011, **257**, 2717–2730.

47 X.-J. Kong, T. He, A. A. Bezrukov, S. Darwish, G.-R. Si, Y.-Z. Zhang, W. Wu, Y. Wang, X. Li, N. Kumar, J.-R. Li and M. J. Zaworotko, Reversible Co(II)–Co(III) Transformation in a Family of Metal–Dipyrazolate Frameworks, *J. Am. Chem. Soc.*, 2024, **146**, 28320–28328.

48 Z. Li, S. Ji, C. Xu, L. Leng, H. Liu, J. H. Horton, L. Du, J. Gao, C. He, X. Qi, Q. Xu and J. Zhu, Engineering the electronic structure of single-atom iron sites with boosted oxygen bifunctional activity for zinc–air batteries, *Adv. Mater.*, 2023, **35**, 2209644.

49 Q. Y. Lu, *ACS Nano*, 2024, **18**, 13973–13982.

50 X. Chen, X. Wang and D. Fang, A review on C1s XPS-spectra for some kinds of carbon materials, *Fullerenes, Nanotubes Carbon Nanostruct.*, 2020, **28**, 1048–1058.

51 M.-Y. Chen, S. Yin, G. Li, J. Chen, W.-Y. Zhao, Y.-K. Lian, H.-R. Wu, W. Yan, J.-N. Zhang and B.-A. Lu, Strong Electronic Metal–Support Interactions Enable the Increased Spin State of Co–N_4 Active Sites and Performance for Acidic Oxygen Reduction Reaction, *ACS Nano*, 2024, **18**, 26115–26126.

52 A. Zitolo, V. Goellner, V. Armel, M.-T. Sougrati, T. Mineva, L. Stievano, E. Fonda and F. Jaouen, Identification of catalytic sites for oxygen reduction in iron- and nitrogen-doped graphene materials, *Nat. Mater.*, 2015, **14**, 937–942.

53 L. Yang, D. Cheng, H. Xu, X. Zeng, X. Wan, J. Shui, Z. Xiang and D. Cao, Unveiling the high-activity origin of single-atom iron catalysts for oxygen reduction reaction, *Proc. Natl. Acad. Sci. U. S. A.*, 2018, **115**, 6626–6631.

54 N. Meng, Y. Feng, Z. Zhao and F. Lian, Boosting the ORR/OER Activity of Cobalt-Based Nano-Catalysts by Co 3d Orbital Regulation, *Small*, 2024, **20**, 2400855.

55 J. Hu, W. Shang, C. Xin, J. Guo, X. Cheng, S. Zhang, S. Song, W. Liu, F. Ju, J. Hou and Y. Shi, Uncovering Dynamic Edge-Sites in Atomic Co–N–C Electrocatalyst for Selective Hydrogen Peroxide Production, *Angew. Chem., Int. Ed.*, 2023, **62**, e202304754.

56 L. Liu, L. Kang, J. Feng, D. G. Hopkinson, C. S. Allen, Y. Tan, H. Gu, I. Mikulska, V. Celorrio, D. Gianolio, T. Wang, L. Zhang, K. Li, J. Zhang, J. Zhu, G. Held, P. Ferrer, D. Grinter, J. Callison, M. Wilding, S. Chen, I. Parkin and G. He, Atomically dispersed asymmetric cobalt electrocatalyst for efficient hydrogen peroxide production in neutral media, *Nat. Commun.*, 2024, **15**, 4079.

57 P. Yin, T. Yao, Y. Wu, L. Zheng, Y. Lin, W. Liu, H. Ju, J. Zhu, X. Hong, Z. Deng, G. Zhou, S. Wei and Y. Li, Single Cobalt Atoms with Precise N-Coordination as Superior Oxygen Reduction Reaction Catalysts, *Angew. Chem., Int. Ed.*, 2016, **55**, 10800–10805.

58 Z. Zhan, J. Yu, S. Li, X. Yi, J. Wang, S. Wang and B. Tan, Ultrathin Hollow Co/N/C Spheres from Hyper-Crosslinked Polymers by a New Universal Strategy with Boosted ORR Efficiency, *Small*, 2023, **19**, 2207642.

59 J. Han, H. Tan, K. Guo, H. Lv, X. Peng, W. Zhang, H. Lin, U.-P. Apfel and R. Cao, The "Pull Effect" of a Hanging ZnII on Improving the Four-Electron Oxygen Reduction Selectivity with Co Porphyrin, *Angew. Chem., Int. Ed.*, 2024, **63**, e202409793.

60 Q. Li, D. Zhang, J. Wu, S. Dai, H. Liu, M. Lu, R. Cui, W. Liang, D. Wang, P. Xi, M. Liu, H. Li and L. Huang, Cation-Deficient Perovskites Greatly Enhance the Electrocatalytic Activity for Oxygen Reduction Reaction, *Adv. Mater.*, 2024, **36**, 2309266.

61 D. Choudhury, R. Das, R. Maurya, G. Gupta and M. Neergat, Low-frequency inductive features in the electrochemical impedance spectra of mass-transport limited redox reactions, *Phys. Chem. Chem. Phys.*, 2023, **25**, 4385–4392.

62 D. Choudhury, R. Das, A. K. Tripathi, D. Priyadarshani and M. Neergat, Kinetics of Hydrogen Evolution Reactions in Acidic Media on Pt, Pd, and MoS_2, *Langmuir*, 2022, **38**, 4341–4350.

63 O. van der Heijden, S. Park, R. E. Vos, J. J. J. Eggebeen and M. T. M. Koper, Tafel Slope Plot as a Tool to Analyze Electrocatalytic Reactions, *ACS Energy Lett.*, 2024, **9**, 1871–1879.

64 S. Yuan, J. Peng, B. Cai, Z. Huang, A. T. Garcia-Esparza, D. Sokaras, Y. Zhang, L. Giordano, K. Akkiraju, Y. G. Zhu, R. Hübner, X. Zou, Y. Román-Leshkov and Y. Shao-Horn, Tunable metal hydroxide–organic frameworks for catalysing oxygen evolution, *Nat. Mater.*, 2022, **21**, 673–680.

65 J. Wang, W. Zang, X. Liu, J. Sun, S. Xi, W. Liu, Z. Kou, L. Shen and J. Wang, Switch Volmer-Heyrovsky to Volmer-Tafel pathway for efficient acidic electrocatalytic hydrogen evolution by correlating Pt single atoms with clusters, *Small*, 2024, 2309427.

66 N. Silva, S. Calderón, M. A. Páez, M. P. Oyarzún, M. T. M. Koper and J. H. Zagal, Probing the $Fe^{n+}/Fe^{(n-1)+}$ redox potential of Fe phthalocyanines and Fe porphyrins as a reactivity descriptor in the electrochemical oxidation of cysteamine, *J. Electroanal. Chem.*, 2018, **819**, 502–510.

67 T. Mineva, I. Matanovic, P. Atanassov, M.-T. Sougrati, L. Stievano, M. Clémancey, A. Kochem, J.-M. Latour and F. Jaouen, Understanding Active Sites in Pyrolyzed Fe–N–C Catalysts for Fuel Cell Cathodes by Bridging Density Functional Theory Calculations and 57Fe Mössbauer Spectroscopy, *ACS Catal.*, 2019, **9**, 9359–9371.

68 M. A. Ahsan, A. R. Puente Santiago, Y. Hong, N. Zhang, M. Cano, E. Rodriguez-Castellon, L. Echegoyen, S. T. Sreenivasan and J. C. Noveron, Tuning of Trifunctional NiCu Bimetallic Nanoparticles Confined in a Porous Carbon Network with Surface Composition and Local Structural Distortions for the Electrocatalytic Oxygen Reduction, Oxygen and Hydrogen Evolution Reactions, *J. Am. Chem. Soc.*, 2020, **142**, 14688–14701.